Exponential time differencing methods with Chebyshev collocation for polymers confined by interacting surfaces

Yi-Xin Liu and Hong-Dong Zhang

Citation: The Journal of Chemical Physics **140**, 224101 (2014); doi: 10.1063/1.4881516
View online: http://dx.doi.org/10.1063/1.4881516
View Table of Contents: http://scitation.aip.org/content/aip/journal/jcp/140/22?ver=pdfcov
Published by the AIP Publishing

Exponential time differencing methods with Chebyshev collocation for polymers confined by interacting surfaces

Yi-Xin Liu (刘一新)[a] and Hong-Dong Zhang (张红东)
State Key Laboratory of Molecular Engineering of Polymers, Department of Macromolecular Science, Fudan University, Shanghai, China

(Received 17 February 2014; accepted 23 May 2014; published online 9 June 2014)

We present a fast and accurate numerical method for the self-consistent field theory calculations of confined polymer systems. It introduces an exponential time differencing method (ETDRK4) based on Chebyshev collocation, which exhibits fourth-order accuracy in temporal domain and spectral accuracy in spatial domain, to solve the modified diffusion equations. Similar to the approach proposed by Hur *et al.* [Macromolecules **45**, 2905 (2012)], non-periodic boundary conditions are adopted to model the confining walls with or without preferential interactions with polymer species, avoiding the use of surface field terms and the mask technique in a conventional approach. The performance of ETDRK4 is examined in comparison with the operator splitting methods with either Fourier collocation or Chebyshev collocation. Numerical experiments show that our exponential time differencing method is more efficient than the operator splitting methods in high accuracy calculations. This method has been applied to diblock copolymers confined by two parallel flat surfaces. © *2014 AIP Publishing LLC*. [http://dx.doi.org/10.1063/1.4881516]

I. INTRODUCTION

Confinement of block copolymers in thin films and other geometries provides a feasible and efficient route to produce novel structures in nanoscale, which are important in a wide range of applications including nanolithography, nanotemplating, nanoporous membranes, coatings, and biomaterials.[1–6] In terms of confinement, it is worth mentioning that polymer brushes obtained by tethering polymer chain ends onto substrates manifest another important example.[7] Significant progresses have been made in understanding the self-assembly of polymers under confinement both experimentally and theoretically. Recent theoretical and numerical studies reveal a number of general principles that govern the structure formation of polymers confined in various geometrical environments.[6,7] Besides those parameters associated with the polymer itself (block volume fractions, Flory-Huggins interaction parameters between different blocks, chain architectures, etc.), putting polymers inside a spatially confined environment introduces new control parameters. Two most important ones are the shape and size of the confining geometry which determine the degree of confinement or the commensurability, and the surface-monomer interactions characterized by the surface affinity. Both parameters strongly influence the structure and the self-assembly behavior of polymers. In particular, the surface affinity not only affects the monomer distribution near the confining walls but also the phase boundaries.

Many theoretical and numerical tools are available to investigate the confining polymer systems, among which the self-consistent field theory (SCFT) is particularly attractive. The numerical SCFT is a method of choice for predicting complex morphologies and the phase diagram of the microphase separations of block copolymers in bulk.[8] It can provide great details about monomer and chain end densities as well as convenient ways to tune almost all parameters. Most importantly, efficient algorithms of the numerical SCFT have been developed to explore both metastable and stable phases. The set of equations encountered in the SCFT are usually solved numerically by an iterative scheme in a self-consistent manner. Among all iterative steps, the most expensive one (at least for neutral polymers) involves the solution of a modified diffusion equation (MDE) for the chain propagator (a probability distribution of polymer segments). Two efficient numerical approaches have emerged: the spectral method introduced by Matsen and Schick[9] and the pseudospectral method introduced by Rasmussen and co-workers.[10,11] The spectral method with poor $O(M^3)$ algorithm complexity, where M is the number of grid points in spectral space, enjoys its high computational efficiency owing to the fact that M can be drastically reduced by incorporating the known symmetry of the phase. The pseudospectral method as a real-space method, on the other hand, is superior when the symmetry of the phase is unknown, or when no symmetry is expected, mainly because of its nearly ideal $O(M \log M)$ algorithm complexity thanks to the usage of the fast Fourier transform (FFT). SCFT calculations of confined polymer systems, where phases are believed to be even more complex and phase structures along the confined direction hardly have any symmetry, prefer real-space methods.

Recently, the numerical SCFT has been applied to confined polymer systems to search for possible morphologies and construct phase diagrams.[12–16] Generally, the confinement is realized by imposing non-periodic boundary conditions other than the periodic boundary condition (PBC) on

[a]Author to whom correspondence should be addressed. Electronic mail: lyx@fudan.edu.cn

the MDE for chain propagators. To model a boundary that is neutral and impenetrable, such as a solid wall without preferential interactions with polymers, the Dirichlet boundary condition (DBC) is often incorporated into the MDE.[17] With this boundary condition on the propagator, a depletion layer forms and the polymer density vanishes at the wall. Sometimes, the Neumann boundary condition (NBC) is used instead of DBC to avoid the depletion layer which may become too sharp to be resolved accurately due to the limit of computation time.[18] Fortunately, MDEs with above two kinds of boundary conditions, if they are homogeneous, can still be solved by the pseudospectral method, provided that the standard Fourier basis (for PBC) is replaced by the sine (for DBC) or cosine (for NBC).[19] However, such Fourier sine (cosine) methods often lose spectral accuracy, i.e., the exponential convergence, since it requires the solution of the MDE is infinite smooth and its all even (odd) derivatives of second and higher order must vanish at the boundary. But these conditions are hardly fulfilled in confined polymer systems. Even worse, these Fourier based methods is not able to handle mixed and Robin boundary conditions (RBC), which are most appropriate for surfaces with preferential affinity.[20,21]

In practice, most of surfaces favor one or more species in a multi-component system and thus exhibit some degree of preferential affinity. To model such surfaces, Matsen[12] developed a masking method which introduces surface field terms to describe the surface affinity and a generalized incompressibility condition (the mask) to preserve the depletion layer of the polymer segment density. This technique allows us to use PBCs and DBCs and avoid the difficulties associated with mixed boundary conditions and RBCs. Consequently, the pseudospectral method is still applicable. However, the numerical SCFT armed with this technique still suffers from same problems faced by the previous numerical SCFT for neutral and impenetrable surfaces, i.e., the difficulty in resolving the sharp depletion layer and loss of accuracy with DBCs. Moreover, the exact form of the mask and the surface field terms are normally specified arbitrary, which is not always irrelevant.[12]

To this end, it highly demands a method that can directly deal with the mixed boundary conditions and RBCs as an alternative to the Fourier based pseudospectral method with or without the mask. We do notice that there is such an attempt. Very recently, Hur *et al.* proposed a pseudospectral method that can handle non-periodic boundary conditions while still preserving the spectral accuracy.[22] The major difference between this method and the conventional pseudospectral method is that Chebyshev polynomials, in place of Fourier bases, are used to approximate spatial functions. Accordingly, an irregular grid consisting of Chebyshev-Gauss-Lobatto (CGL) points, which distribute more densely near the boundary, is used. Chebyshev collocation enables solution of the MDE subject to non-periodic boundary conditions with exponential convergence. And it permits rapid transformations from the physical space to the spectral space and vice versa in debt to the availability of FFTs. In this method, the operator splitting (OS) algorithm is applied as in the conventional pseudospectral method. But it costs additional operations because the Laplacian term is not diagonal in the transformed Chebyshev space. In particular, to represent the Laplacian term in the spectral space, the authors used a Padé approximation to re-express the Laplacian term in a form with consistent second order accuracy in the contour step. Then, pairs of Helmholtz-type equations are solved for each contour step, which needs $O(48M)$ operations. Note the large coefficient before the linear term. For Helmholtz equation subject to mixed boundary conditions and RBCs, linear complexity is also possible but it requires an even larger coefficient. Probably due to this reason, the surface affinity was modeled by the masking method other than RBCs in their studies. Moreover, although it is possible to improve the contour stepping accuracy by higher order OS algorithm, more and more Helmholtz pairs should be solved. For example, for a fourth-order splitting scheme, there are seven Laplacian terms to be evaluated in comparison to one for the second order scheme. Nevertheless, it is necessary to develop higher order algorithms for stepping along the contour to achieve the demanded accuracy with bigger contour step.

Here, we propose a competitive fourth order accurate algorithm for solving the MDEs that can treat non-periodic boundary conditions efficiently and consistently. Chebyshev collocation is also used to preserve spectral accuracy. Unlike the pseudospectral method utilizing the OS algorithm, we introduce an exponential time differencing (ETD) scheme to approximate the time differential and a fourth order Runge-Kutta scheme (RK4) for the time stepping. The algorithm details about the ETDRK4 method and the numerical SCFT scheme is described in Sec. III. The performance of the ETDRK4 method is addressed in Secs. IV and V. In Sec. VI, we present applications of the ETDRK4 SCFT method on diblock copolymers confined by two parallel flat interacting surfaces.

II. THEORETICAL FORMULATION

A. SCFT for diblock copolymers under confinement

For AB diblock copolymers under confinement, the set of SCFT equations are the same as those of diblock copolymers in bulk. The only difference between bulk and confined SCFT in present formulation lies in the boundary conditions of the MDEs which will be addressed later on. Below we summarize the main SCFT equations for an canonical ensemble of n AB diblock copolymers with N segments in total, of which the A and B blocks consist of fN and $(1-f)N$ segments, respectively. Starting from the partition function and utilizing the Hubbard-Stratonovich transformation, one obtains the Helmholtz free energy in the mean-field approximation (in units of $k_{\mathrm{B}}T$)

$$F = \int d\mathbf{r}\Big[\chi\phi_A(\mathbf{r})\phi_B(\mathbf{r}) - w_A(\mathbf{r})\phi_A(\mathbf{r}) - w_B(\mathbf{r})\phi_B(\mathbf{r}) + \frac{\xi}{2}\left[\phi_A(\mathbf{r}) + \phi_B(\mathbf{r}) - 1\right]^2\Big] - \ln Q[w_A, w_B] \qquad (1)$$

with the position vector $\mathbf{r}$ rescaled by R_g and segment densities ϕ_K $(K = \mathrm{A}, \mathrm{B})$ rescaled by the average segment density ρ_0, where $R_g = a\sqrt{N/6}$ is the radius of gyration of an unperturbed AB block copolymer with a being the Kuhn

length. The Flory-Huggins interaction parameter χ in the above equation describes the interaction energy between A and B segments. In Eq. (1), w_A and w_B are auxiliary potential fields generated by A and B blocks, and Q represents the normalized single chain partition function. The term containing ξ describes a penalty for local density fluctuations away from the average segment density,[8,23] which is introduced to make current formulation compatible with various boundary conditions. The parameter ξ describes the strength of the harmonic energy penalty thus its reciprocal ξ^{-1} measures the compressibility of the model. This model approaches the incompressible model in the limit $\xi \to \infty$.

The set of SCFT equations are given by

$$w_A(\mathbf{r}) = \chi N \phi_B(\mathbf{r}) + \xi N \left[\phi_A(\mathbf{r}) + \phi_B(\mathbf{r}) - 1\right], \quad (2)$$

$$w_B(\mathbf{r}) = \chi N \phi_A(\mathbf{r}) + \xi N \left[\phi_A(\mathbf{r}) + \phi_B(\mathbf{r}) - 1\right]. \quad (3)$$

These equations should be solved in a self-consistent manner since ϕ_A and ϕ_B implicitly depend on w_A and w_B. The segment densities for A and B segments can be evaluated from chain propagators q_A, q_B, and corresponding complementary propagators q_A^*, q_B^*,

$$\phi_A(\mathbf{r}) = \frac{1}{Q}\int_0^f ds\, q_A(\mathbf{r}, s) q_A^*(\mathbf{r}, f-s), \quad (4)$$

$$\phi_B(\mathbf{r}) = \frac{1}{Q}\int_0^{1-f} ds\, q_B(\mathbf{r}, s) q_B^*(\mathbf{r}, 1-f-s). \quad (5)$$

The chain propagators $q_K(\mathbf{r}, s)$, $K = \mathrm{A}, \mathrm{B}$, which give the probability to find segment s at position $\mathbf{r}$, satisfy the following MDE:

$$\frac{\partial q_K(\mathbf{r}, s)}{\partial s} = \nabla^2 q_K - w_K(\mathbf{r}) q_K, \quad (6)$$

with initial condition $q_A(\mathbf{r}, 0) = 1$ for chain propagator of A block and $q_B(\mathbf{r}, 0) = q_A(\mathbf{r}, f)$ for chain propagator of B block. The complementary propagators $q_K^*(\mathbf{r}, s)$ also satisfy Eq. (6) but subject to different initial conditions: $q_A^*(\mathbf{r}, 0) = q_B^*(\mathbf{r}, 1-f)$ and $q_B^*(\mathbf{r}, 0) = 1$. The normalized single chain partition function Q can also be obtained from the propagator as $Q(\mathbf{r}, [w_A, w_B]) = V^{-1}\int d\mathbf{r}\, q_B(\mathbf{r}, 1-f)$ with V the dimensionless volume of the system.

B. Modelling interacting surfaces

In this study, we are interested in situations where polymer chains cannot explore the full space freely; they are confined by impenetrable surfaces outside of which the probability to find a polymer segment vanishes. As discussed in the Introduction, to model the confinement effect, it is sufficient to impose appropriate boundary conditions on the chain propagators.[8] For neutral, impenetrable surfaces, a convenient choice is to use the DBC. To be compatible with the incompressible model or to avoid resolving sharp boundary layers of concentrated polymer solutions and polymer melt, the DBC has to be replaced by the NBC. For surfaces that interact with polymer segments, previous numerical studies often use the DBC in combination with a surface potential where the DBC ensures the segment density vanishes at the boundary and the surface potential models the surface affinity. As this approach may suffer from devoting too much computation force on resolving the surface potential near the boundary, here we adopt the approach as suggested by Fredrickson[8] for numerical studies which replaces the surface potential with an effective boundary condition. For weakly attractive walls, de Gennes[21] has proposed an appropriate boundary condition,

$$\frac{\partial q}{\partial n} + \kappa q = 0 \quad \text{at the boundary}, \quad (7)$$

where $\partial q/\partial n$ denotes the normal derivative at the boundary, and $|\kappa| k_B T$ gives a measure of the binding energy per polymer chain at the surface. Thus, $|\kappa|^{-1}$ is a length scale that characterizes the net strength of the attractive interaction. The boundary condition in Eq. (7), so called the RBC, reduces to the DBC when $|\kappa| \to \infty$ and it reduces to the NBC when $\kappa = 0$.

To be specific, in this study we consider the situation where the melt is confined by two parallel flat surfaces located at $z = 0$ and $z = D$. Then the boundary conditions become

$$\frac{\partial q_K}{\partial z} \pm \kappa_{jK} q_K = 0, \quad (8)$$

for $K = \mathrm{A}, \mathrm{B}$, and $j = a, b$, where a and b stand for the $z = 0$ and $z = D$ boundaries, respectively. The plus and minus signs are chosen for κ_a and κ_b, respectively, due to the opposite sign of the normal derivative at the two boundaries. The surface affinity parameter κ_{jK} being positive means that confining walls attract polymer segments of K blocks while negative parameters indicate that confining walls prefer polymer segments not from K blocks. To reduce the number of parameters, we introduce an additional condition,[8] $\kappa_{jA} f + \kappa_{jB}(1-f) = 0$, for $j = a, b$, so that $\kappa_a = \kappa_{aA}$ and $\kappa_b = \kappa_{bA}$ are the left control parameters.

III. NUMERICAL METHODS

In this study, the set of SCFT equations listed in Sec. II A are solved by a standard real-space iterative scheme as described in Ref. 8. In this scheme, a continuous steepest descent scheme using the explicit Euler formula is used to relax an arbitrary initial configuration of the potential field $w_K(\mathbf{r})$ to a local solution.[8] The segment density $\phi_K(\mathbf{r})$ is evaluated by a Simpson's rule. The Clenshaw-Curtis quadrature used by Ref. 22 is adopted to evaluate the normalized single chain partition function Q and the free energy F on the CGL grid.

The solution of the MDE lies in the heart of this scheme—it usually dominates the computational cost. Here, an efficient algorithm, the ETDRK4 method on CGL grid, which is spectrally accurate in spatial discretization and fourth order accurate in time discretization, is devised to solve MDEs involving non-periodic boundary conditions. For the sake of comparison, the operator splitting methods on equispaced grid presented in Ref. 19 and the operator splitting methods on CGL grid (OSCHEB) proposed by Hur *et al.*[22] are also implemented. Note that the operator splitting methods on equispaced grid are only applicable to DBC and NBC. The one applicable to DBC requires sine basis (OSS) while the other applicable to NBC requires cosine basis (OSC).

To efficiently handle non-periodic boundary conditions, we discretize spatial variables on a CGL grid with a set of points

$$z_j = \cos\left(\frac{\pi j}{N_z}\right), \quad j = 0, 1, \ldots, N_z. \tag{9}$$

Obviously, these Chebyshev points distribute irregularly on the line segment, $z \in [-1, 1]$, and are clustered near the two boundaries at $z = -1$ and $z = 1$. The actual range along z dimension, $[0, L_z]$, can be projected onto the interval $[-1, 1]$ through a linear transform $z\prime = 2z/L_z - 1$. Then the MDE is solved by the ETDRK4 method, which has been shown to perform extremely well in solving diffusion type problems.[24]

A. ETDRK4 on the CGL grid

The ETDRK4 algorithm is an exponential time differencing method based on Runge-Kutta time stepping. Here, we closely follow the treatment of Cox and Matthews[25] but with some further improvements. We first write the MDE in a general form $\partial q/\partial s = \mathcal{L}q + \mathcal{F}(q)$, where $\mathcal{L} = \partial^2/\partial z^2$ is an elliptic operator and $\mathcal{F} = -w(\mathbf{r})q$. Once we discretize the spatial part of the MDE we get a system of ODEs,

$$\frac{\partial q}{\partial s} = \mathbf{L}q + \mathbf{F}(q, s), \tag{10}$$

where $\mathbf{L}$ and $\mathbf{F}$ are matrix representations for $\mathcal{L}$ and $\mathcal{F}$, respectively. Multiplying both sides of Eq. (10) with $\exp(-\mathbf{L}s)$ and integrating over a single contour step from $s = s_n$ to $s = s_{n+1} = s_n + h$, we get

$$q(s_{n+1}) = e^{\mathbf{L}h} q(s_n) + e^{\mathbf{L}h} \int_0^h d\tau\, e^{\mathbf{L}\tau} \mathbf{F}[q(s_n + \tau), s_n + \tau]. \tag{11}$$

Various ETD schemes come from the approximations to the integral in the above equations. In this study, we employ the scheme of Krogstad[26] with formulae given by

$$a_n = \varphi_0(\mathbf{L}h/2)q_n + \frac{h}{2}\varphi_1(\mathbf{L}h/2)\mathbf{F}(q_n), \tag{12a}$$

$$b_n = a_n + h\varphi_2(\mathbf{L}h/2)[\mathbf{F}(a_n) - \mathbf{F}(q_n)], \tag{12b}$$

$$c_n = \varphi_0(\mathbf{L}h)q_n + h\varphi_1(\mathbf{L}h)\mathbf{F}(q_n) + 2h\varphi_2(\mathbf{L}h)[\mathbf{F}(b_n) - \mathbf{F}(q_n)], \tag{12c}$$

$$q_{n+1} = c_n + h[4\varphi_3(\mathbf{L}h) - \varphi_2(\mathbf{L}h)][\mathbf{F}(q_n) + \mathbf{F}(c_n)] + 2h\varphi_2(\mathbf{L}h)\mathbf{F}(a_n) - 4h\varphi_3(\mathbf{L}h)[\mathbf{F}(a_n) + \mathbf{F}(b_n)], \tag{12d}$$

where h and $\mathbf{I}$ are the time step and the identity matrix, respectively. The above scheme is based on Runge-Kutta time stepping which is fourth order accurate in this particular form. The coefficients in the above equations are defined by $\varphi_{l+1}(z) = [\varphi_l(z) - 1/l!]/z$ with $l = 0, 1, 2$ and $\varphi_0(z) = \exp(z)$. Then the remaining tasks are construction of matrix $\mathbf{L}$ and evaluation of these coefficients. With all related matrices and coefficients in hand, the ETDRK4 algorithm is merely several matrix-vector products (each product may cost $O(N_z^2)$ operations for an $N_z \times N_z$ matrix) in each time stepping. In our case, we choose $h = \Delta s = 1/N_s$ with N_s the number of steps along the chain contour.

B. Construction of matrix L

To construct $\mathbf{L}$ on the CGL grid, we approximate the function $q(z)$ by a truncated Chebyshev polynomial expansion, $q(z) \approx \sum_{n=0}^{N_z} a_n T_n(z)$ where $T_n(z) = \cos(nz)$ is the Chebyshev polynomial. Using the idea of collocation, the derivatives of $q(z)$ with respect to z could be obtained from the Chebyshev differentiation matrix $\mathbf{D}$ whose elements are given by[27]

$$D_{jk} = \frac{\gamma_j}{\gamma_k}\frac{(-1)^{j+k}}{z_j - z_k} \quad \text{for } j \neq k, \tag{13a}$$

$$D_{jj} = -\sum_{j \neq k=0}^{N_z} D_{jk} \quad \text{for } j \neq 0, N_z, \tag{13b}$$

$$D_{00} = -\frac{2N_z^2 + 1}{6}, \quad D_{N_z N_z} = \frac{2N_z^2 + 1}{6}, \tag{13c}$$

where $\gamma_j = 2$ if $j = 0$ or N_z, otherwise $\gamma_j = 1$. $\mathbf{D}$ can be viewed as a higher order operator (global, using all grid points) to compute the first order derivative of a function in contrast to the finite difference scheme (local, using only neighboring grid points). Note that $\mathbf{D}$ is an $(N_z + 1) \times (N_z + 1)$ matrix. Consequently, we can now construct $\mathbf{L}$ from $\mathbf{D}$ as long as appropriate boundary conditions are incorporated. For DBCs, it is no need to solve the MDE on the boundaries because we know the function values on the boundaries. For NBCs and RBCs, the function values on the boundaries are unknown and we shall solve them together with the interior values. Below we state how to incorporate various boundary conditions into the matrix $\mathbf{L}$.

1. Homogeneous DBCs

Homogeneous DBC occurs when both κ_a and κ_b go to infinity or equivalently, $q(z_0) = 0$ and $q(z_{N_z}) = 0$. Then the MDE has only $N_z - 1$ unknowns: $q(z_1), q(z_2), \ldots, q(z_{N_z - 1})$. The elements of matrix $\mathbf{L}$ are given by

$$L_{ij} = \sum_{k=0}^{N_z} D_{ik} D_{kj}, \tag{14}$$

for $i, j = 1, 2, \ldots, N_z - 1$, meaning that the matrix $\mathbf{L}$ is the sub-matrix of $\mathbf{D}^2$ whose first and last rows and columns are deleted.

2. Homogeneous RBCs and homogeneous NBCs

The case of homogeneous RBCs occurs when $\kappa_a \kappa_b \neq 0$. The matrix $\mathbf{L}$ is given by

$$L_{ij} = \sum_{k=0}^{N_z} D_{ik} \hat{D}_{kj}, \quad j = 1, 2, \ldots, N_z - 1, \tag{15a}$$

$$L_{ij} = \sum_{k=0}^{N_z} D_{ik}\hat{D}_{k0} - \kappa_b D_{i0}, \quad j = 0, \tag{15b}$$

$$L_{ij} = \sum_{k=0}^{N_z} D_{ik}\hat{D}_{kN_z} - \kappa_a D_{iN_z}, \quad j = N_z, \tag{15c}$$

where $\hat{D}_{ij} = 0$ if $i = 0$ or N_z, otherwise $\hat{D}_{ij} = D_{ij}$. In practice, to obtain the matrix $\mathbf{L}$ one first computes the matrix product $\mathbf{D}\hat{\mathbf{D}}$, then subtracts $\kappa_b D_{i0}$ and $\kappa_a D_{iN_z}$ from its first and last columns, respectively.

The homogeneous NBC is a special case of RBC. One can see this by setting $\kappa_a = \kappa_b = 0$. The above algorithm is also applicable to the mixed NBC-RBC case by setting either κ_a or κ_b to 0 at the NBC boundary.

3. Mixed DBC and RBC

Mixed DBC and RBC occurs when one of the boundary conditions is DBC. Unfortunately, application of the similar approaches for homogeneous DBCs and RBCs on this case fails during our numerical experiments. We thus employ an alternative method proposed by Weideman and Reddy[28] based on Hermite interpolation, which is an extension of Lagrange interpolation that enables one to incorporate derivative values in addition to function values.[29]

For DBC-RBC (the boundary condition at $z = z_{N_z}$ is DBC), it can be shown that the interpolant of degree $N_z + 1$ below:

$$p_{N_z+1} = \sum_{j=0}^{N_z-1} q(z_j)\tilde{\phi}_j(z)$$

satisfies the interpolation conditions, $p_{N_z+1}(z_j) = q(z_j)$, $j = 0, 1, \ldots, N_z - 1$ as well as the boundary conditions. The modified polynomials are given by

$$\tilde{\phi}_0(z) = \left[1 - \left(\frac{\partial}{\partial z}\phi_0(z_0) + \kappa_b\right)(z-1)\right]\phi_0(z), \tag{16a}$$

$$\tilde{\phi}_j(z) = \frac{1-z}{1-z_j}\phi_j(z), \quad j = 1, 2, \ldots, N-1, \tag{16b}$$

where $\phi_j(z)$ on the CGL grid are defined as

$$\phi_j(z) = \frac{(-1)^{j+1}}{\gamma_j}\frac{1-z^2}{N_z^2}\frac{T'_{N_z}(z)}{z - z_j}$$

for $j = 0, 1, \ldots, N_z - 1$, where $\gamma_j = 2$ if $j = 0$ or N_z, otherwise $\gamma_j = 1$. It is now straightforward to find the matrix $\mathbf{L}$,

$$L_{ij} = \frac{\partial^2}{\partial z^2}\tilde{\phi}_j(z_i), \quad i, j = 0, 1, \ldots, N_z - 1. \tag{17}$$

The quantities $\frac{\partial^2}{\partial z^2}\tilde{\phi}_j(z_i)$ may be expressed explicitly in terms of the quantities $\frac{\partial^2}{\partial z^2}\phi_j(z_i)$, which are the entries of the second-order Chebyshev differentiation matrix $\mathbf{D}^2$.

The matrix $\mathbf{L}$ for RBC-DBC is obtained by replacing ϕ_0 and z_0 with ϕ_{N_z} and z_{N_z} in Eq. (16a), respectively. As NBC is a special case of RBC, the matrix $\mathbf{L}$ for DBC-NBC and NBC-DBC is obtained by setting $\kappa_b = 0$ in DBC-RBC and $\kappa_a = 0$ in RBC-DBC, respectively.

C. Evaluation of coefficients φ_l

For small z, direct computation of the coefficients, such as $\varphi_1(z) = (e^z - 1)/z$, suffers from disastrous cancellation errors.[24] To overcome such vulnerability, Schmelzer and Trefethen[30] proposed a powerful technique using the complex contour integral

$$\varphi_l(\mathbf{L}) = \frac{1}{2\pi i}\int_\Gamma \frac{e^\tau}{\tau^l}(\tau\mathbf{I} - \mathbf{L})^{-1}d\tau, \tag{18}$$

where Γ can be any contour in the complex plane that encloses the eigenvalues of $\mathbf{L}$. Contour integral of analytic functions in the complex plane is easy to evaluate by means of the trapezoidal rule, which converges exponentially.[30] Since the MDEs are diffusion type equations, most of eigenvalues lie on the negative real axis. Therefore, a hyperbolic contour, which encloses the whole negative real axis, is a good choice.

Here, we employ a hyperbola suggested by Weideman and Trefethen,[31] $v = \mu[1 + \sin(iu - \alpha)]$ $(-\infty < u < \infty)$ where v is a complex number whose real and imaginary parts determine a hyperbolic contour in the complex plane. μ and α are two constants which control the width and asymptotic angle of the hyperbola. Applying the trapezoidal rule to evaluate the integral, we have

$$\varphi_l(\mathbf{L}h) = \frac{\mu\Delta}{2\pi}\sum_{k=-M}^{M}\frac{e^{v_k h}}{(v_k h)^l}(v_k\mathbf{I} - \mathbf{L})^{-1}\cos(iu_k - \alpha), \tag{19}$$

where $2M + 1$ is the number of equally spaced points on the contour and their spacing is $\Delta = 1.0818/M$, and $u_k = k\Delta$ and $v_k = v(u_k)$. According to Weideman and Trefethen,[31] we choose $\mu = 4.4921M/h$ and $\alpha = 1.1721$ which optimize the accuracy of Eq. (19).

The accuracy of this complex contour integral methods depends on M and the eigenvalues of $\mathbf{L}h$. Generally, the larger the eigenvalues, the bigger M is required to retain the same level of accuracy. It is known that the largest eigenvalue of matrix $\mathbf{L}$ $(N_z \times N_z)$ in this study scales as $-N_z^4$. Therefore, the accuracy of coefficients φ_l degrades quickly when we increase the spatial resolution N_z but keep M fixed. The lost of accuracy of φ_l will further propagate to the ETDRK4 method causing serious decrease of the accuracy of the final solution, which is termed as "over-resolution" problem.

For non-diagonal problems such as the matrix $\mathbf{L}$ in this study, we need evaluation of M matrix inverse, which is expensive. However, as this is done just once before the time-stepping begins, the impact on the total computing time should be negligible.

D. Two-dimensional (2D) and three-dimensional (3D) calculations

The 1D ETDRK4 method described in Secs. III A–III C can be generalized to enable calculations in higher dimensions. For AB diblock copolymers confined by two parallel flat surfaces, it becomes particular simple because they are not confined in the other two dimensions and the periodic boundary conditions can be imposed.

Here, we take 2D calculations as an example. By performing Fourier transform in x direction, Eq. (6) becomes

$$\frac{\partial \hat{q}(k_x, z)}{\partial s} = \left(-k_x^2 + \frac{\partial^2}{\partial z^2}\right)\hat{q}(k_x, z) + \hat{f}(q), \tag{20}$$

where $\hat{q}$ and $\hat{f}$ denote the Fourier transform of functions $q(x, z)$ and $f(x, z) = -w(x, z)q(x, z)$ along x dimension, respectively. In practice, $\hat{f}$ is obtained by first computing $f(x, z)$ in the real space and then performing an FFT on $f(x, z)$ along x dimension. Since in each time stepping $\hat{q}$ is actually computed, we have to perform an additional inverse FFT whenever q is needed. We collocate functions on an equispaced grid $\mathbf{x} = (x_0, x_1, \ldots, x_{N_x-1})^T$ where $x_i = iL_x/N_x$. L_x and N_x are the length of the calculation cell and the number of grid points, respectively. Accordingly, the spectral collocation points are $k_{x,0}, k_{x,1}, \ldots, k_{x,N_x-1}$ with $k_{x,i} = 2\pi i/L_x$. It then follows that for each wavenumber $k_{x,i}$, there is a 1D MDE to be solved:

$$\frac{\partial \hat{q}_i(z)}{\partial s} = \left(-k_{x,i}^2 + \frac{\partial^2}{\partial z^2}\right)\hat{q}_i(z) + \hat{f}_i(q) \tag{21}$$

for $i = 0, 1, \ldots, N_x - 1$, where $\hat{q}_i(z) = \hat{q}(k_{x,i}, z)$ and $\hat{f}_i(z) = \hat{f}(k_{x,i}, z)$. The above equation can be solved by the same ETDRK4 method as long as one replaces $\mathbf{L}$ with $\mathbf{L} - k_{x,i}^2\mathbf{I}$. Therefore, the total computation cost should be approximately N_x times larger than the 1D method. The 3D calculations are almost identical to the 2D calculations except that an additional dimension (y direction) should be taken into account, which can be treated similarly as the x dimension. Extensions to other regular geometries are possible.[32]

IV. PERFORMANCE OF THE ETDRK4 METHOD

In this section, we conduct a comparison of the performance of the ETDRK4 method, the OSS method, and the OSCHEB method. Instead of carrying out the whole SCFT calculations, the 1D MDE is numerically solved with a given potential field $w(z) = 1 - 2\,\mathrm{sech}^2[(6z - 3L_z)/4]$ which is adopted from the book by Fredrickson.[8] The length of the calculation cell L_z is set to 10.0 for all calculations. It should be noted that this particular potential field is relatively simple as compared to the self-consistent field generated by self-assembly of block copolymers. Thus, it may require higher spatial and/or temporal resolution to obtain same lever of accuracy. The initial condition is $q(z, 0) = 1$, for $0 < z < L_z$. The MDE is solved subject to the homogeneous DBCs.

The error is estimated by the relative error in the normalized single chain partition function, $|Q - Q^*|/|Q^*|$, where Q is the computed value and Q^* is the "exact" value. Q is computed by numerically integrating the equation $Q = \int_0^{L_z} dz\, q(z, 1)$ using the Clenshaw-Curtis quadrature scheme[22,27] or the trapezoidal rule to the CGL grid (for ETDRK4 and OSCHEB) or the equispaced grid (for OSS), respectively.

It is critical to obtain the exact solution of the MDE for error analysis. Unfortunately, the analytical solution of the MDE with the given potential field is unavailable. As a common approach we take the numerical solution obtained by the OSCHEB method using $N_z = 8192$, $N_s = 2 \times 10^5$ as the "exact" solution, which will be used for all error analysis below.

A. Convergence in N_s

In this part, the effect of contour step $\Delta s = 1/N_s$ on the accuracy of the calculations is analyzed. We carried out a series of numerical experiments with various contour step for fixed spatial discretization number N_z. The results are shown in Figure 1, which reveal that the ETDRK4 methods are superior to both OSS and OSCHEB methods in two aspects. First, the ETDRK4 method is more accurate for all spatial resolution given the same contour step. In Figure 1(c), we find that

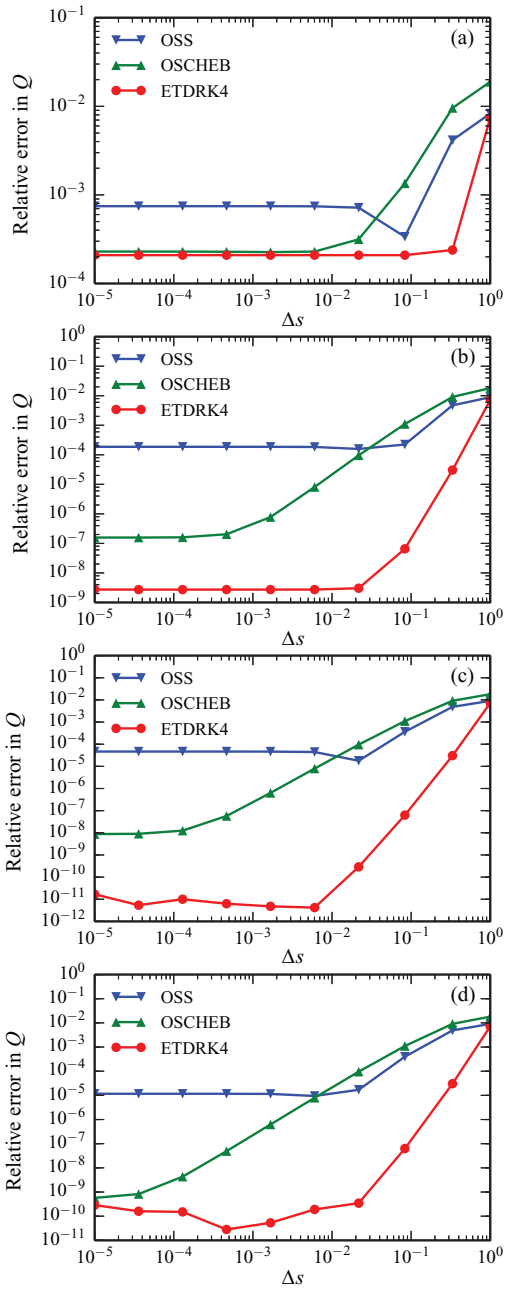

FIG. 1. Relative error in the normalized single chain partition function Q for the OSS, OSCHEB, and ETDRK4 solutions of the MDE as a function of the contour step Δs at fixed N_z with values of (a) 32, (b) 64, (c) 128, and (d) 256.

the error of the ETDRK4 methods is down to 10^{-11} at $\Delta s \approx 0.01$, while the error of both OSS and OSCHEB methods is larger than 10^{-5}. Moreover, the flatten of the error profiles of OSS and OSCHEB methods at low Δs region implies that it is hardly possible to make errors less than 10^{-9} and 10^{-5} by decreasing Δs for the OSS and OSCHEB methods, respectively. Second, the error of the ETDRK4 methods decreases much faster than the other two methods for fixed spatial resolution. The fourth-order convergence rate in time stepping is confirmed by the slope of the linear part of the error profile of the ETDRK4 methods, while the error of the OSS and OSCHEB methods decreases only as $O(\Delta s^2)$.

Comparing the four plots in Figure 1, we also notice that the accuracy of both OSS and OSCHEB methods improves as the increase of N_z, while the accuracy of the ETDRK4 methods is worse at $N_z = 256$ than that at $N_z = 128$, which indicates that the ETDRK4 method may suffer from the over-resolution problem. Therefore, practically it is important to keep the spatial resolution in a suitable region for the ETDRK4 methods.

B. Convergence in N_z

In this part, we examine the convergence properties of the ETDRK4, OSS, and OSCHEB methods with respect to the spatial resolution. Two sets of numerical experiments have been done for various spatial resolution by fixing contour steps at $\Delta s = 10^{-5}$. As shown in Figure 2(a), the Chebyshev calculations including the ETDRK4 and OSCHEB methods exhibit a much more sharper decrease of the error than that of the OSS method. In the log-log plot of the error as a function of N_z, the error of the OSS method decreases linearly and the slope is -1.993 obtained by a linear fit of the linear part of the OSS profile in Figure 2(a), suggesting that this method is only second-order accurate in spatial resolution.

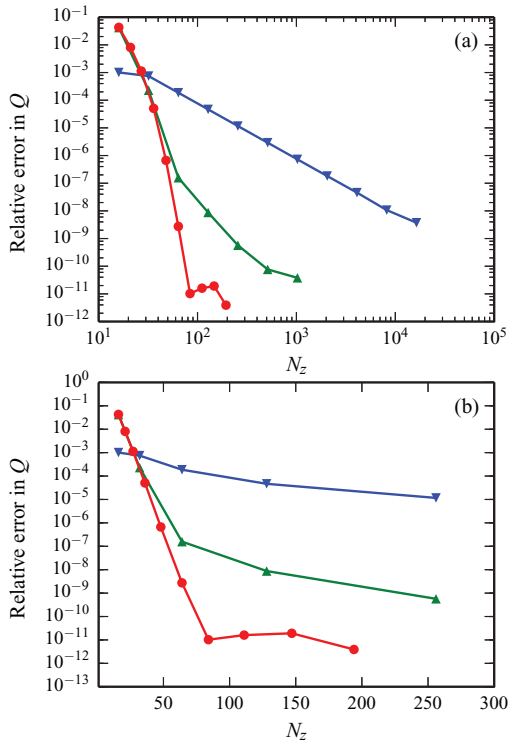

FIG. 2. The relative error in Q as a function of spatial resolution N_z at fixed contour step $\Delta s = 10^{-5}$. Down triangle: OSS; up triangle: OSCHEB; disk: ETDRK4. The function is plotted in (a) log-log scale, and (b) semilog scale. Note the different range of N_z in these two plots.

By plotting the error in semilog scale as shown in Figure 2(b), it becomes clear that the ETDRK4 and OSCHEB methods both converge exponentially (linear decrease of the error in the semilog plot indicates the exponential convergence), as expected. However, the OSCHEB method begins to lose the spectral accuracy at $N_z = 64$, much earlier than the ETDRK4 method which begins at $N_z = 128$. Consequently, the ETDRK4 method can reach much better accuracy than the OSCHEB method for a fixed contour step size. Note that $N_z = 128$ is the spatial resolution that the ETDRK4 method begins to suffer from the over-resolution problem. It means that the ETDRK4 method could retain the spectral convergence property until the over-resolution problem occurs.

C. Computational cost

We compare the computation cost of various MDE solvers with respect to the spatial resolution by counting the computation time. All methods are implemented in Python and timing results were collected with the aid of the Python package `cProfile`. All benchmarks were performed on a 2.50 GHz Intel Xeon CPU and the results are presented in Figure 3.

Since the initialization of ETDRK4 involves evaluation of RK coefficients φ_l, which costs significant amount of time when N_z is large. Apart from the total computation time, the "core" computation time which excludes the initialization contribution is also reported. As can be seen in Figure 3(a), for the OSS and OSCHEB methods the total computation time and the "core" computation time are almost identical, while for the ETDRK4 method they differs in nearly an order of magnitude. Fortunately, for SCFT calculations the initialization is only done once before the relaxation procedures. Therefore, the impact of this initialization becomes less and less important when the number of iterations gets larger. This fact should be made clear in Sec. V.

Figure 3(a) shows that the OSS method is the fastest method thanks to the utilization of the FFTs. The profile becomes linear for large N_z which agrees with its computational complexity $O(N_z \ln N_z)$. Although the OSCHEB method shares the same complexity as the OSS method, it costs much more time. It implicates that the coefficient preceded the complexity of the OSCHEB method is very large. For small and modest value of N_z, the coefficient is relatively large that the computational cost of the OSCHEB method exceeds that of the ETDRK4 method which has complexity $O(N_z^2)$ in theory. For conventional SCFT calculations, the relevant value of N_z ranges from tens to several hundreds. This value also lies in the practical region. For N_z larger than 10^3, the computation time for both OSCHEB and ETDRK4 methods quickly grows to a prohibited amount.

The above benchmark only gives a crude impression on the performance of the three algorithms. Although OSS is

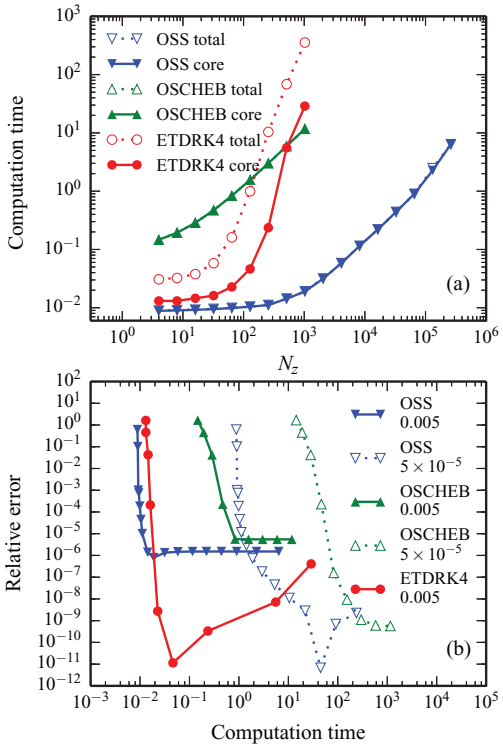

FIG. 3. (a) Computation time as a function of spatial resolution N_z for algorithms OSS, OSCHEB, and ETDRK4. The contour step Δs is fixed. "Total" means the total time for a full solution while "core" means the computation time excluding the initialization before actual time stepping. Note that for both OSS and OSCHEB, the total time and the core time of both OSS and OSCHEB are so close that their corresponding symbols are superimposed. (b) Relative error in Q as a function of "core" computation time for algorithms OSS, OSCHEB, and ETDRK4. Different computation times correspond to different spatial resolution which can be read from (a). The number after the algorithm name in the figure legend stands for contour step size.

faster than OSCHEB and ETDRK4 for the same spatial resolution and contour step size, it has been shown that it converges only as N_z^{-2} as compared to the spectral convergence of the other two. Thus, to achieve the same accuracy as OSCHEB and ETDRK4 methods, the OSS method needs to be done with much higher spatial resolution as well as a much smaller contour step size. Therefore, it is expected that the OSS method could be less efficient than the other two algorithms. A better way to address the efficiency of these algorithms is to plot the error as a function of the "core" computation time. Such a plot is shown in Figure 3(b) where the solid symbols are obtained by numerically solving the MDEs with contour steps fixed at 5×10^{-3}. To reduce the error in fixed contour step size, one needs to increase the spatial resolution leading to the increase of the computation time. For all three algorithms, the error first decreases with the computation time. For low accuracy calculations (the error larger than 10^{-6}), the OSS method is the most efficient one. However, the best accuracy can be achieved by both OSS and OSCHEB methods is only 10^{-6}. Further increase of the computation time hardly improves the accuracy. On the contrary, the ETDRK4 method can further reduce the error to 10^{-11} with a computation time which is comparable to the cost of the OSS method for the accuracy of 10^{-6}. The increase of error for last three data points of ETDRK4 is caused by the over-resolution problem because we did not raise the number of points in the complex contour when we evaluate the ETDRK4 coefficients with large N_z.

To improve the accuracy of the OSS and OSCHEB methods to the level of the best accuracy of the ETDRK4 method, we must drastically reduce the contour step size which costs tremendous amount of the computation time. In Figure 3(b), the results of the OSS and OSCHEB methods with $\Delta s = 5 \times 10^{-5}$ are also presented. With this tiny contour step size, the error of the OSS and OSCHEB methods can indeed be reduced to the magnitude of 10^{-10}. However, the computational time is several orders of magnitude larger than that of the ETDRK4 method. Combining all the above facts, we could safely conclude that the ETDRK4 method is the method of choice for obtaining high accuracy solution of the MDEs. Even for low accuracy calculations, it is still better than the OSCHEB method. One would also expect that above conclusion is still valid for calculations in higher dimensions where polymers are confined in one dimension requiring only 1D ETDRK4.

V. PERFORMANCE OF FULL SCFT CALCULATIONS

In this section, we compare the computational efficiency of the full SCFT calculations utilizing the OSCHEB and ETDRK4 methods. 1D numerical experiments are done for homopolymer brushes grafted onto flat surfaces subject to homogeneous DBCs. The total computation time, the time consumed by solving MDEs, and the time cost of the initialization are summarized in Figure 4. In both OSCHEB and ETDRK4 SCFT calculations, the solution of the MDEs is the most time-consuming step, as indicated by the fact that the total and MDE computation times are almost identical for both methods (see Figure 4). The relatively larger initialization time of the ETDRK4 method is due to the evaluation of the RK coefficients. Note that the initialization is only done once for each SCFT calculation, meaning that its computation time does not vary with the number of SCFT iterations. Therefore, the importance of the initialization diminishes considerably in a practical SCFT calculation, where 10^2–10^3 iterations are required. For all spatial resolutions ($N_z \leq 2048$)

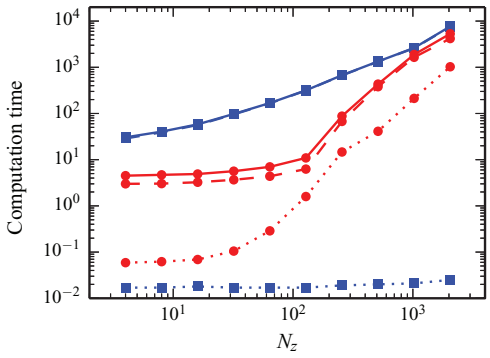

FIG. 4. Computation time for performing 100 SCFT iterations as a function of spatial resolution with the OSCHEB and ETDRK4 algorithms. Both boundaries are DBCs. Square: OSCHEB; disk: ETDRK4; dotted line: initialization; dashed line: MDE; solid line: total.

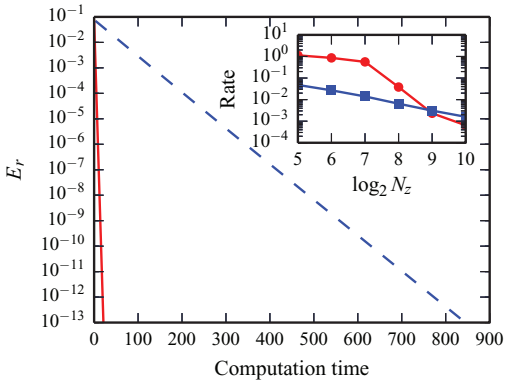

FIG. 5. The development of the residual error of SCFT calculations of polymer brushes with computation time which excludes the initialization procedure for the ETDRK4 and OSCHEB methods. Both boundaries are DBCs. For the main plot, N_z and Δs are fixed at 128 and 0.005, respectively. The inset figure plots the decreasing rate of the residual error as a function of the spatial resolution. The solid line in the main plot and the disk symbol in the inset plot are for the ETDRK4 method, while others are for the OSCHEB method.

we tested, the ETDRK4 SCFT calculations consume less time than the OSCHEB SCFT calculations.

Based on above benchmark results, it is not conclusive enough to determine which algorithm is more efficient. A more practical way to assess the efficiency of the two algorithms is to compare the computation time required to achieve a given accuracy. In Figure 5, we plot the residual error of the SCFT equation of homopolymer brush system as a function of computation time which excludes the initialization procedure for the ETDRK4 and OSCHEB methods at $N_z = 128$ and $\Delta s = 0.005$. The error of both methods decreases linearly in the semilog plot, meaning that the SCFT algorithms converge exponentially. Although the ETDRK4 and the OSCHEB SCFT methods both give spectral accuracy, the decreasing rate of the former is much faster than the latter. We also plot the decreasing rate of the error, which is the absolute value of the slope obtained by a linear fit of the error profile, for both methods as a function of the spatial resolution in the inset of Figure 5. As can be seen, for $N_z < 512$ which is the spatial resolution of practical importance, the decreasing rate of the ETDRK4 SCFT algorithm is much larger than that of the OSCHEB algorithm.

VI. APPLICATION IN AB DIBLOCK COPOLYMERS CONFINED BY INTERACTING SURFACES

Block copolymers belong to an important class of polymeric materials that can self-assemble into complex microstructures on the scale of 10 to 100 nm, making them an ideal candidate for nanotechnologies. Confining block copolymers in two parallel interacting surfaces introduces two new parameters, namely, the surface interactions between polymer segments and confining surfaces and the commensurability which describes how well the film thickness matches the natural period of the block copolymers in bulk. The competition between these two factors may lead to even richer microstructures which have been revealed by both experimental and theoretical studies. Among various theoretical and numerical methods, SCFT has been proven to be a powerful tool in prediction of microphase morphologies of block copolymers both in bulk and under confinement. A common approach to describe the surface interactions between polymers and confining surfaces is the introduction of surface fields to the SCFT equations combined with appropriate boundary conditions, usually DBCs. The form of the surface fields is chosen mainly based on numerical considerations. However, these surface details are not completely irrelevant and their effects should be addressed carefully as suggested by Ref. 12. Fortunately, our ETDRK4 SCFT method circumvents this difficulty by replacing the surface fields with appropriate boundary conditions.

In this part, we demonstrate the feasibility of our ETDRK4 SCFT method using the same example as Ref. 12, where lamellar forming AB diblock copolymers ($f = 0.5$) at an intermediate degree of segregation ($\chi N = 20$) are confined by two parallel flat surfaces with either symmetric or anti-symmetric surface affinities. The commensurability parameter, D/L_0, is fixed at 1.2, where $L_0 = 4.044R_g$ is the period of the lamellar structures in bulk.[12] At this commensurability, the domain spacing of parallel lamellae will be significantly frustrated for both symmetric and anti-symmetric surface affinities, the ideal film thicknesses correspond to which should be mL_0 and $(m + 1/2)L_0$ with integer m, respectively. Therefore, at weak surface affinities the frustrating effect overwhelms the gain of energy by covering preferred blocks on the walls, leading to perpendicular orientation of the lamellae.

Figure 6 shows calculated possible morphologies through initializing the fields w_A and w_B with random configurations and varying the surface affinities. Parallel lamellae are

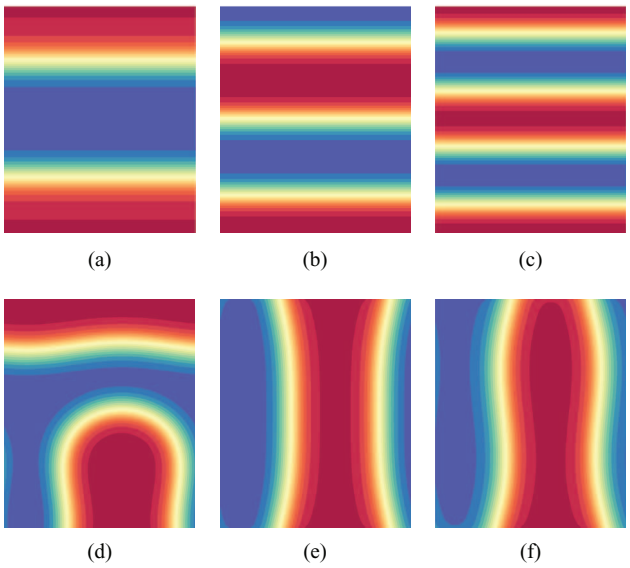

FIG. 6. Possible morphologies of symmetric AB diblock copolymers confined by two flat surfaces with distance fixed at $D/L_0 = 1.2$ at segregation $\chi N = 20$, calculated by the ETDRK4 SCFT method with random initializations. The size of the calculation box is $N_x = 64$ and $N_z = 32$. Top and bottom edges in each plot are confining walls. Morphologies in each plot are denoted as (a) $L_2^{\parallel}$, (b) $L_3^{\parallel}$, (c) $L_4^{\parallel}$, (d) L_1^{M}, and (e) and (f) $L_{\perp}$. In (a)–(e), both walls attract A blocks; in (f) the top and bottom walls attract B and A blocks, respectively. Red and blue represent the A-rich and B-rich domains, respectively.

denoted by $L_\nu^{||}$ with ν the number of the A/B interfaces (see Figures 6(a)–6(c)), while $L_\perp$ denotes the perpendicular lamellae (Figures 6(e) and 6(f)). Only one mixed lamellar morphology containing a parallel layer (L_1^M) appears in the random initiation calculations. We noticed that the perpendicular lamellae both in $L_\perp$ and L_1^M phases are curved, in consistent with previous SCFT calculations and Monte Carlo simulations.[12,14,33] In Figure 6(d), both surfaces attract A blocks, and thus A segments tend to wet both surfaces, leading to contact angles less than 90° for A-rich domains. According to our numerical results, the contact angle decreases with the increase of the surface affinity. Finally, the near surface part of A-rich domains merges together with the neighboring A-rich domains to form a continuous wetting layer on both surfaces. For antisymmetric surface affinities, such as that in Figure 6(f), the contact angle of the A-rich domain on the top surface where it prefers B blocks becomes larger than 90°. The behavior of the contact angle should be well explained by Young's equation as demonstrated by Hur *et al.*[22]

To determine which phase is stable for AB diblock copolymers confined by two surfaces with symmetric surface affinities, the fields corresponding to the phases shown in Figures 6(a)–6(e) are used as initial input for SCFT calculations. After the calculations converge, the free energy of each phase is plotted as a function of the surface affinity ($\kappa_a = \kappa_b$) shown in Figure 7. It is now clear that at weak surface affinities, the perpendicular lamellae are stable while $L_2^{||}$ is the stable phase at strong surface affinities. The intersection of the $L_2^{||}$ and $L_\perp$ curves around $\kappa_a = 0.57$ indicates an order-order transition point. Matsen[12] calculated a similar plot but at a different commensurability where $L_2^{||}$ and $L_4^{||}$ are equal in free energy. In their plot, $L_2^{||}$ and $L_4^{||}$ share a common curve and the free energy curve of $L_\perp$ bends down at strong surface potential. And there is no intersection of the $L_2^{||}$ and $L_\perp$ curves. At the commensurability $D/L_0 = 1.2$ studied here, $L_2^{||}$ and $L_4^{||}$ split into two approximately parallel curves and the free energy of $L_\perp$ changes little with the surface affinity.

As in the study of Ref. 12, the slope of the free energy curve can be roughly understood by the strong-segregation theory (SST). The slope is given by $2(1 - \psi_a - \psi_b)/D$, where ψ_a is the fraction of A segments at $z = 0$ surface and ψ_b is the same for that at $z = D$ surface. In both $L_2^{||}$ and $L_4^{||}$, both walls are covered by A blocks leading to $\psi_a \approx \psi_b \approx 1.0$, which produces identical negative slopes. On the other hand, $\psi_a = \psi_b = 0.5$ at $\kappa_a = 0$ in $L_\perp$ gives zero slope. Further increase of κ_a should attract more A blocks onto the walls (note the curvature of the A-rich domain near the walls in Figure 6(e)), which may result in a slightly negative slope. However, this effect is far less significant here than that in the study of Matsen.[12] The slope of L_1^M in Figure 7 is about a half of the slopes of $L_2^{||}$ and $L_4^{||}$. It can be explained similarly that $\psi_a \approx 0.5$ for the wall covered by perpendicular domains and $\psi_b \approx 1.0$ for the wall covered by parallel A-rich domain. Finally, in $L_3^{||}$ phase $\psi_a \approx 1.0$ while $\psi_b \approx 0$, and therefore the slope is almost zero in consistent with the calculation results.

SCFT calculations have not been performed for anti-symmetric surface affinities in the study of Matsen.[12] Based on SST calculations, the author argued that L_ν^M phases are unstable for anti-symmetric surface affinities. Using our ET-DRK4 SCFT methods, we have performed calculations at the commensurability $D/L_0 = 1.2$ and the results are presented in Figure 8. The surface affinities are chosen to be equal in strength, i.e., $\kappa_a = -\kappa_b$. Since the L_1^M phase is asymmetric along the wall normal direction, it exists two configurations for anti-symmetric surface affinities: L_1^{Ma} and L_1^{Mb}. The parallel A-rich domain covers the wall that attracts A blocks in L_1^{Ma} while in L_1^{Mb} the perpendicular domains cover the wall that attracts A blocks. In Figure 8, we find that L_1^{Ma} is more stable than L_1^{Mb} and its free energy curve has a negative slope rather than a positive one like L_1^{Mb}. The difference of the sign of the slopes of these two phases are well explained by the SST formula mentioned above by noticing that $\psi_a \approx 1.0$ and $\psi_b \approx 0.5$ in L_1^{Ma} phase while $\psi_a \approx 0.5$ and $\psi \approx 0$ in L_1^{Mb}. The stability relation between L_1^{Ma} and L_1^{Mb} implies that perpendicular domains contribute less than parallel domains in reducing free energy by covering attractive surfaces. Both L_1^{Ma} and L_1^{Mb} phases are less stable than the $L_3^{||}$ and $L_\perp$ phases in the whole range of surface affinities we studied, agreeing with the assertion of Matsen.[12] Moreover, there is also an order-order transition from $L_\perp$ to $L_3^{||}$ by enhancing the surface affinities.

Two-dimensional calculations are sufficient for above lamella-forming diblock copolymers, while cylinder-forming and other asymmetric block copolymers require three-dimensional calculations to reveal additional information in

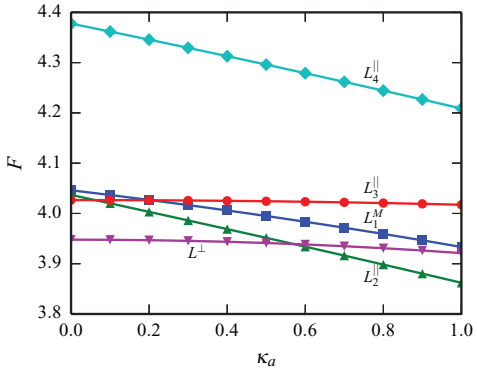

FIG. 7. Free energies F of the phases shown in Figures 6(a)–6(e) as a function of surface affinity κ_a. Both walls have the same surface affinities, i.e., $\kappa_a = \kappa_b$. The lateral size has been adjusted to obtain the lowest free energy.

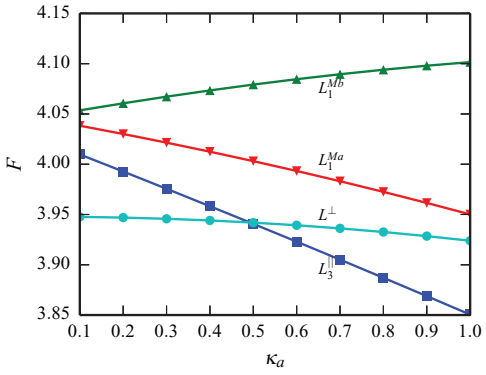

FIG. 8. Similar to Figure 7 except that anti-symmetric surface affinities ($\kappa_a = -\kappa_b$) are considered.

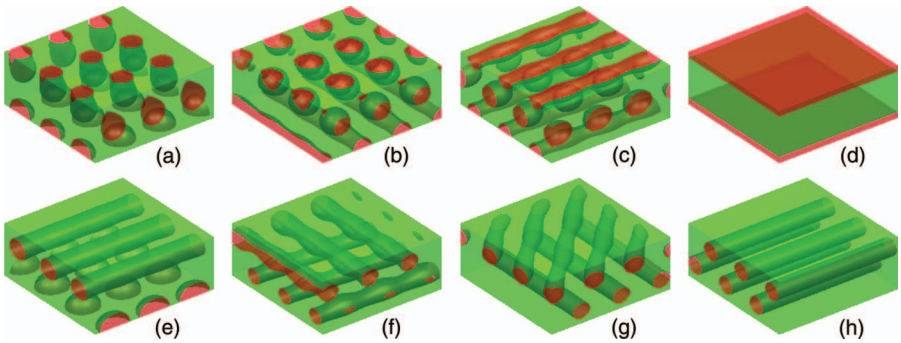

FIG. 9. Possible morphologies of cylinder-forming AB diblock copolymers ($f = 0.2$) confined by two flat surfaces with distance fixed at $D/L_0 = 1.2$ at segregation $\chi N = 40$, calculated from the ETDRK4 SCFT method with random initialization. The size of the calculation box is $N_x = N_y = 32$ and $N_z = 24$. The physical size of both lateral dimensions are L_0. Top and bottom surfaces in each plot are confining walls. In (a)–(d), both walls attract A blocks; in (e)–(h) both walls attract B blocks. The surface affinities are (a) $\kappa_a = 0$, (b) $\kappa_a = 0.1$, (c) $\kappa_a = 0.2$, (d) $\kappa_a = 0.3$, (e) $\kappa_a = -0.1$, (f) $\kappa_a = -0.2$, (g) $\kappa_a = -0.3$, and (h) $\kappa_a = -0.5$. Red and green represent the A-rich and B-rich domains, respectively. Each plot is obtained by repeating the calculation box three times in x and y dimensions.

another lateral dimension. For example, it is possible that the lamellar structures in 2D systems are actually cylinders in 3D systems.[34] As the simplest model system of cylinder-forming block copolymers under confinement, diblock copolymers confined by two parallel flat surfaces can form various microstructures by tuning the film thickness, the surface affinity, and the corresponding control parameters in bulk. Possible (stable and metastable) structures include parallel/perpendicular cylinders, lamellae, spheres between two wetting layers of preferred blocks, cylinders between two layers of half cylinders, and perforated lamellae, as reported in both experimental and theoretical studies.[16,35]

Using our ETDRK4 SCFT method with random initialization, we have identified several interesting metastable microstructures by sweeping the surface affinity κ_a from -5.0 to 5.0. The calculations were performed for a diblock copolymer ($f = 0.2$) at strong segregation ($\chi N = 40$) confined by two parallel flat surfaces with symmetric affinities, which forms a cylindrical phase with a spacing $L_0 = 4.30R_g$ between the centers of neighboring cylinders in bulk.[13] Figure 9 summarizes all structures in the numerical results. In addition to lamellae and parallel cylinders, we observe a set of hybrid structures including perpendicular cylinders plus a layer of half spheres (Figure 9(a)), a layer of half spheres and a layer of half cylinders on surfaces plus a layer of spheres in between (Figure 9(b)), two layers of half cylinders on surfaces with a layer of spheres in between (Figure 9(c)), a layer of half spheres on surface plus a layer of cylinders (Figure 9(e)), and two layers of cylinders with different orientations (Figures 9(f) and 6(g)).

For surfaces that attract A blocks, A segments tend to distribute on the surfaces. But at weak surface affinities, the gain of free energy by covering A segments is so small that the distribution of A segments in the interior is also possible, just like the mixed lamellar morphologies of the symmetric diblock copolymers. At strong surface affinities ($\kappa_a > 0.4$), all calculations with random initiation result in lamellae, strongly implying that the lamellar phase is the stable phase in this case. As the case of surfaces attracting B blocks, two layers of cylinders with different orientations (parallel/orthogonal/diagonal) randomly occur for different surface affinities. The occurrence of non-parallel cylinders may be due to the constraint of the lateral size, which should be varied to relax the pseudo-stress. Therefore, we believe that the stable phase is parallel cylinders at strong surface affinities in this case.

Heckmann and Drossel[34] found that numerical inaccuracies are not negligible in determination of stable phases. In their study, the perforated lamellae lose their stability by merely increasing the number of collocation points, which clearly shows the influence of the accuracy of the numerical algorithm. Therefore, to determine the stable phase in 3D space, one should choose more accurate algorithms. Our ETDRK4 SCFT method serves as a good candidate because it is a promising method that delivers high accuracy in solution of the MDEs.

VII. CONCLUSION

In summary, we have shown that the exponential time differencing method on CGL grid, ETDRK4, is a powerful tool for solving MDE with non-periodic boundary conditions. It exhibits fourth order accuracy in time (contour) stepping as compared to the second order accuracy often found in the literature. It retains spectral accuracy for non-periodic problems as those pseudospectral methods for periodic problems. And it outperforms a similar Chebyshev based algorithm devised by Hur *et al.* in the convergence rate with respect to number of grid points. The ETDRK4 method has been successfully incorporated into the standard SCFT algorithm and its performance is addressed. The ETDRK4 SCFT algorithm also retains the exponential convergence rate. Using this method, we can reproduce the results in the literature in higher accuracy with less contour steps and fewer grid points. Equivalently, to achieve the same accuracy, our ETDRK4 SCFT method costs less computation time thus is more efficient.

To demonstrate the power of our ETDRK4 SCFT method, we apply it to solve the SCFT equations of diblock copolymers confined by interacting surfaces. For diblock copolymers confined by two parallel surfaces, 2D and 3D calculations are performed for symmetric and cylinder-forming diblock copolymers, respectively. At low surface affinities

perpendicular lamellae are stable phases for symmetric diblock copolymers, while parallel lamellae $L_2^{\parallel}$ (symmetric surface affinity) and $L_3^{\parallel}$ (anti-symmetric surface affinity) become stable when the surface affinity exceeds a transition value. The mixed lamellar phase is proved to be metastable for both symmetric and anti-symmetric surface affinities. For cylinder-forming diblock copolymers, our ETDRK4 SCFT calculations revealed several novel hybrid structures at low surface affinities. This method can be readily extended to any non-periodic problems provided that polymers are confined in regular geometries such as disk, cylinder, and sphere in addition to parallelepiped.

ACKNOWLEDGMENTS

This work is supported by the National Natural Science Foundation of China (Grant No. 21004013), the Fundamental Research Funds for the Central Universities, and the National Basic Research Program of China (Grant No. 2011CB605701).

[1]M. J. Fasolka and A. M. Mayes, Annu. Rev. Phys. Chem. **31**, 323 (2001).
[2]C. Park, J. Yoon, and E. L. Thomas, Polymer **44**, 6725 (2003).
[3]I. W. Hamley, Prog. Polym. Sci. **34**, 1161 (2009).
[4]J. N. L. Albert and T. H. Epps, Mater. Today **13**, 24 (2010).
[5]C. R. Stewart-Sloan and E. L. Thomas, Eur. Polym. J. **47**, 630 (2011).
[6]A.-C. Shi and B. Li, Soft Matter **9**, 1398 (2013).
[7]K. Binder and A. Milchev, J. Polym. Sci., Part B: Polym. Phys. **50**, 1515 (2012).
[8]G. H. Fredrickson, *The Equilibrium Theory of Inhomogeneous Polymers* (Clarendon Press, Oxford, 2006).
[9]M. W. Matsen and M. Schick, Phys. Rev. Lett. **72**, 2660 (1994).
[10]G. Tzeremes, K. Rasmussen, T. Lookman, and A. Saxena, Phys. Rev. E **65**, 041806 (2002).
[11]K. Rasmussen and G. Kalosakas, J. Polym. Sci., Part B: Polym. Phys. **40**, 1777 (2002).
[12]M. W. Matsen, J. Chem. Phys. **106**, 7781 (1997).
[13]W. Li and R. A. Wickham, Macromolecules **39**, 8492 (2006).
[14]D. Meng and Q. Wang, Soft Matter **6**, 5891 (2010).
[15]P. Chen, H. Liang, R. Xia, J. Qian, and X. Feng, Macromolecules **46**, 922 (2013).
[16]W. Li, M. Liu, and F. Qiu, J. Phys. Chem. B **117**, 5280 (2013).
[17]A. Alexander-Katz, A. G. Moreira, and G. H. Fredrickson, J. Chem. Phys. **118**, 9030 (2003).
[18]S. T. Milner and D. C. Morse, Phys. Rev. E **54**, 3793 (1996).
[19]T. L. Chantawansri, S.-M. Hur, C. J. García-Cervera, H. D. Ceniceros, and G. H. Fredrickson, J. Chem. Phys. **134**, 244905 (2011).
[20]D. T. Wu, G. H. Fredrickson, and J.-P. Carton, J. Chem. Phys. **104**, 6387 (1996).
[21]P. G. de Gennes, *Scaling Concepts in Polymer Physics* (Cornell University Press, Ithaca, 1979).
[22]S.-M. Hur, C. J. García-Cervera, and G. H. Fredrickson, Macromolecules **45**, 2905 (2012).
[23]E. Helfand, J. Chem. Phys. **62**, 999 (1975).
[24]A. K. Kassam and L. N. Trefethen, SIAM J. Sci. Comput. **26**, 1214 (2005).
[25]S. M. Cox and P. C. Matthews, J. Comput. Phys. **176**, 430 (2002).
[26]S. Krogstad, "Topics in numerical Lie group integration," Ph.D. thesis (The University of Bergen, 2003).
[27]L. N. Trefethen, *Spectral Methods in MATLAB* (SIAM, Philadelphia, 2000).
[28]J. A. C. Weideman and S. C. Reddy, ACM Trans. Math. Software **26**, 465 (2000).
[29]W. Huang and D. Sloan, SIAM J. Numer. Anal. **29**, 1626 (1992).
[30]T. Schmelzer and L. N. Trefethen, Electron. Trans. Numer. Anal. **29**, 1 (2007).
[31]J. A. C. Weideman and L. N. Trefethen, Math. Comput. **76**, 1341 (2007).
[32]Taking cylinder as an example, the MDE becomes $\frac{\partial q(r,\theta,z)}{\partial s}=(\frac{\partial^2}{\partial r^2}+\frac{1}{r}\frac{\partial}{\partial r}+\frac{1}{r^2}\frac{\partial^2}{\partial \theta^2}+\frac{\partial^2}{\partial z^2})q-w(r,\theta,z)q$ in the cylindrical coordinate. Functions in θ dimension are naturally periodic. Further assuming functions in z dimension are also periodic, one can solve this MDE using 1D ETDRK4 method for r dimension.
[33]T. Geisinger, M. Müller, and K. Binder, J. Chem. Phys. **111**, 5251 (1999).
[34]M. Heckmann and B. Drossel, Macromolecules **41**, 7679 (2008).
[35]Q. Wang, P. F. Nealey, and J. J. de Pablo, Macromolecules **34**, 3458 (2001).